Appl. Phys. A (2016) 122:418
DOI 10.1007/s00339-016-9948-3

Applied Physics A
Materials Science & Processing

Effect of Ni and Au ion irradiations on structural and optical properties of nanocrystalline Sb-doped SnO_2 thin films

Feroz A. Mir[1,3] · **Khalid Mujasam Batoo**[2]

Received: 27 January 2015 / Accepted: 29 February 2016 / Published online: 17 March 2016

Abstract The effect of shift heavy ion irradiations on the structural and optical properties of 6 % Sb-doped SnO_2 thin films deposited on quartz substrate by electron beam evaporation technique is presented. Two ion species Ni and Au with energy 120 MeV and fluence of 1×10^{13} ion/cm^2 were used. These films were characterized by X-ray diffraction, atomic force microscope, UV–visible and micro-Raman spectroscopy. From structural analysis, these films exhibit tetragonal rutile structure and retain it even after irradiation. The ion irradiations have shown improvement in the structural properties, such as increase in grain size and decrease in the lattice strain. Raman study also indicates enhancement in quality of crystal structure after irradiations. The grain growth after ion interaction is also observed by atomic force microscope study. Further, a variation in optical band gap and reduction in disorder is observed after irradiation. Other parameters such as Urbach tails energy and steepness parameter are obtained from optical data. The overall observed physical properties show a significant improvement after irradiation. A good correspondence between structures with its various properties can be seen.

✉ Khalid Mujasam Batoo
khalid.mujasam@gmail.com

[1] University Science Instrumentation Centre, University of Kashmir, Srinagar, J&K 190006, India

[2] King Abdullah Institute for Nanotechnology, King Saud University, PO Box 2455, Riyadh 11451, Kingdom of Saudi Arabia

[3] Present Address: Department of Nuclear Medicine, Sher-i-Kashmir Institute of Medical Sciences, Srinagar, J&K 190011, India

1 Introduction

Nanomaterials have attracted great interest of researchers not only by their unique chemical and physical properties, but also due to their potential application in many fields, which has stimulated the search for new synthetic methods for these materials. For last few decades, oxide-based semiconductors are at center stage due to their unique potential properties (such as optical, magnetic and electrical), and among them, Tin dioxide is among the dominant ones [1]. Bulk SnO_2 crystallizes in the tetragonal rutile type structure (known in its mineral form as cassiterite), *P42/mnm* space group with two Sn and four oxygen atoms per unit cell. The lattice parameters are $a = b = 0.4737$ nm, $c = 0.3185$ nm. SnO_2 is an important n-type wide-energy-gap semiconductor ($E_g = 3.64$ eV, 300 K) with high carrier concentration (6×10^{20} cm^{-3}) which shows its scope for various potential applications such as in gas sensors [2], transparent conducting electrodes [3], Li batteries [4] and optoelectronic devices [5]. During the past decade, SnO_2-based nanostructures have been one of the most important oxide nanostructures due to their properties and potential applications [6, 7].

Sb-doped SnO_2 (antimony tin oxide = ATO) film is an important transparent conducting material because of its numerous applications such as in solar cells, liquid crystal displays, low-emissivity architectural glass, photodetectors and video touch screens [1–4]. ATO film can be fabricated by various techniques including electron beam evaporation [5], chemical vapor deposition [6], spray pyrolysis [7], sputtering [8] or sol–gel [9]. Each of these methods has its own advantages and disadvantages. Few above-mentioned techniques required vacuum and few required solution processing. The ultimate goal is to get best quality films for need-based applications. Special treatments under

controlled conditions are carried out to get these desired properties, and list includes annealing in different background gases to ion beam irradiations [10].

Swift heavy ion (SHI) beam is a unique tool to modify the properties of the materials and makes it attractive for industrial applications. When SHI beam passes through a material, energetic ions loose their energy mainly via two mechanisms called electronic energy loss (Se) and nuclear energy loss (Sn). These two mechanisms are independent of each other. When the energy of SHI is transferred to the nucleus of the target material via elastic collisions with the atoms, the energy loss mechanism is called nuclear energy loss, which is dominant in the lower energy region (1 keV/amu) and when SHI beam makes inelastic collisions with the electronic subsystem of the atom of the target material, and then, energy is transferred to the lattice by electron–phonon coupling which in turn modify the material, process is called electronic energy loss. The electronic energy loss is dominant in the case of high-energy region (1 MeV/amu) [10, 11]. Mohanty et al. [12] studied the formation of tin oxide nanocrystals in e-beam evaporated thin films on different substrates induced by SHI irradiation. Gas sensing properties of SHI irradiated sol–gel prepared tin oxide thin films have been investigated by Rani et al. [13]. Deshpande et al. [14] studied the effect of 100 MeV Au ions on tin oxide films prepared by MSILAR technique. Effect of 120 MeV Au ions on various properties of tin oxide films deposited on glass substrate was also studied [15]. Sharma et al. [16] also studied the effect of 100 MeV Oxygen ions on optical properties of SnO_2 thin films. However, the systematic study of SHI irradiation-induced modifications in Sb-doped SnO_2 thin films has not been carried out so far. Therefore, it is interesting to irradiate and study the modifications induced in transparent and conducting properties of Sb–SnO_2 thin films by SHI.

2 Experimental

Sb–SnO_2 films of 200 nm thickness were deposited by electron beam evaporation system on fused quartz substrates maintained at 300 °C. The Sb–SnO_2 powder pellet with a composition of 6 wt% Sb_2O_3 and 94 wt% SnO_2 was used as the evaporation source material. The substrate-to-target distance was 10 cm. Before starting the evaporation processes, a steady-state chamber pressure of about 10^{-6} Torr was obtained. The deposition rate (0.3 nm/s) and the film thickness were controlled and monitored during the evaporation process by using a quartz crystal sensor.

The crystal structure of these films was characterized by X-ray diffractometer (Philips X'pert) with Ni-filtered Cu K_α-radiation ($\lambda = 1.54056$ Å) in the diffraction angle (2θ) range 20–80° with a step size of 0.05 (2θ/s). Optical absorbance spectra were obtained on an ultraviolet–visible–near infrared (UV–Vis–NIR) spectrophotometer (Varian Cary 5000) in the wavelength range 200–800 nm. The Raman analysis was made by micro-Raman (Renishaw, UK) using Ar ion laser with 532 nm wavelength. The surface morphology was observed with the help of atomic force microscope (AFM) (Veeco, USA) in tapping mode. All structural and optical measurements of these samples were carried out at ambient temperature (300 K).

The irradiation experiment of these films was carried out by using 15UD Pelletron tandem accelerator at Inter University Accelerator Center (IUAC), New Delhi, India. During irradiation, the beam current was kept around one particle nanoampere (pnA). Ion beam was focused to a spot of around 1 mm diameter and then scanned over 1 cm^2 area using magnetic scanner. The present high energy was chosen to have the range of the ions few microns (more than thickness of film), so that no ions are implanted in the film.

The following ion beams were applied for modification:

- 120 MeV Ni fluence 1×10^{13} ions cm^{-2}
- 120 MeV Au fluence 1×10^{13} ions cm^{-2}

The various ion irradiation parameters were determined by using SRIM code (version 2006) [17] and are presented in Table 1. The S_e and S_n represent the electronic and nuclear stopping powers, respectively, and R_p is the projected range of the ions.

3 Results and discussion

3.1 Structural analysis

Figure 1 shows the XRD pattern of unirradiated and irradiated Sb–SnO_2 thin films. The XRD data of Sb–SnO_2 films revealed peaks at 30.48°, 37.95° and 62.38° corresponding to the (110), (200) and (310) planes, respectively. All the prominent peaks in the pattern correspond to the tetragonal (rutile) structure of SnO_2 and are indexed on the JCPDS file no. 031116. It is also noticed that after Sb doping in SnO_2 matrix, no impurities were detected in the product. It means that the SnO_2 structures were pure tetragonal rutile structure. However, with radiation, an increase in intensity of the peaks was observed. The observed sharp peak can be related to increase in particle size.

The lattice parameters a and c (by analyzing XRD data) of pristine and irradiated films have been calculated by using the following relation and are given in Table 2.

$$1/d^2 = \left(h^2 + k^2\right)/a^2 + l^2/c^2 \quad (1)$$

Table 1 Various SRIM parameters for these irradiated films

Ion	Electronic energy loss (Se) eV/Å	Nuclear energy loss (Sn) eV/Å	Range (μm)
Au	1527.7133	28.492	15.02
Ni	847.231	1.4976	20.35

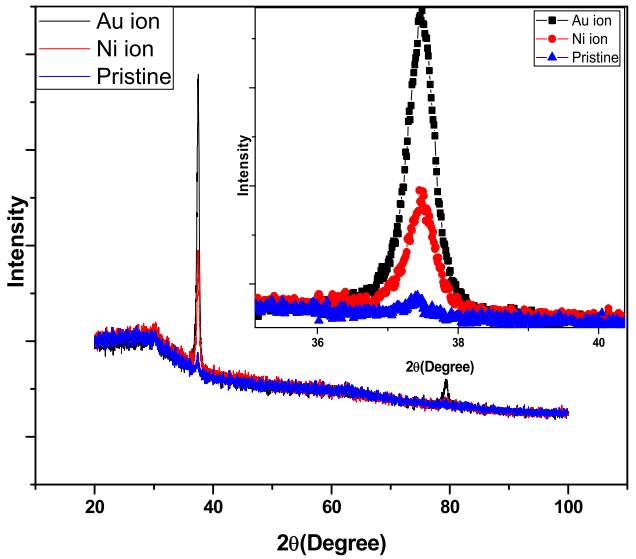

Fig. 1 XRD pattern of Pristine, Ni and Au ion irradiated films. *Inset* shows variation in (200) peak

where d is lattice spacing and h, k and l are Miller indices. The d values has been estimated from (110) peak for different ion irradiations of Sb–SnO_2 films. Here it should be note that the lattice parameters (a and c) calculated from the XRD patterns for the SnO_2:Sb films given in Table 2 are larger than those of the JCPDS of pure SnO_2 powder. Since Sn^{4+} and Sb^{5+} have different covalent and ionic radii [Sn^{4+} (0.72 A) and Sb^{5+} (0.62 A)], and assuming that Sn substitution by Sb would generate oxygen vacancies to keep charge neutrality, a well-noticed lattice distortion would be expected if solid solution between the compositions was formed [18]. [This increase in lattice parameters may also be related to oxygen deficiency and strain effects due to the thermal effect expansion coefficient mismatch between the film (7.2×10^{-6}/ °C) and glass substrate (4.6×10^{-6}/ °C)].

It has been observed that the d(110) value shows some variations with different ion beam (Table 2). The variations observed in lattice parameters are considerably small. However, dealing with films, these variations can be considered due to micro-strains-inducing lattice compression due to lattice mismatch and by energetic ion irradiations [19–21].

Using the diffraction lines of the (110) plane, the crystallite or particle size is estimated by Scherer equation [22]:

$$D = 0.94\lambda/\beta \cos\theta \quad (2)$$

where λ is the X-ray wavelength (1.543 Å for Cu K_α), β (full width at half maximum) $= (\beta_M^2 - \beta_i^2)^{1/2}$. β_M and β_i are the measured and instrumental broadening in radians, respectively, and θ is the Bragg's angle in degrees. The calculated average grain size for Sb–SnO_2 film is about ~11.76 nm. As mentioned above, the basic rutile phase remains practically same after irradiation, but the average particle size increases with irradiations.

Narrowing of peaks also reflects the decrease in the concentration of lattice imperfection due to the increase in the internal micro-strain within the matrix [23]. Similar results were also reported by other workers [24]. Basically the grain size maximizes the imperfect regions of the matrix and is further supported by the smaller strain and dislocation densities.

Further the strain (ε) was calculated by using the following formula [22]:

$$\varepsilon = [(\lambda/D\cos\theta) - \beta]/\tan\theta \quad (3)$$

The dislocation density (δ) which represents the amount of defects in the films is calculated using the formula [22]:

$$\delta = 15\,\varepsilon/a\,D \quad (4)$$

As observed here, the calculated strain slightly decreases after irradiations (see Table 2). Further, there is decrease in dislocation density after irradiations. The decrease in dislocation density might be due to decrease in the number of grain boundaries resulting from the increase in grain size. Table 2 shows that ion irradiations have decreased the lattice strain, which shows that crystalline lattice of Sb–SnO_2 thin films has been relaxed. However,

Table 2 Various structural parameters of the Pristine, Ni and Au ion irradiated films

Sample	Grain size (nm)	Strain (ε) ($line^{-2}$ m^{-4})	Dislocation density δ × 10^{15} (line/m^2)	Orientation index (ϕ)	Lattice parameter (Å) a	Lattice parameter (Å) c
Virgin	20.36	0.09637	2.412	2.28	4.750	3.193
Au ion irradiated	21.48	0.09137	2.167	2.27	4.751	3.195
Ni ion irradiated	21.54	0.09112	2.155	2.53	4.753	3.197

strain reduced after irradiations are confirming the enhancement in crystallinity and reduction in disorder in the system (evident from increase in peak intensity). It seems that the release of observed strain by SHI irradiation leads to the growth of *a*-axis-oriented rutile SnO_2 crystallites.

The stress (σ) developed was calculated by the relation given below:

$$\sigma = \varepsilon E \tag{5}$$

where E is the Young's modulus, for SnO_2 and its value is 295.8 GPa [25].

The intensity peak of (110) plane reflection increases with increase irradiating ion mass (Fig. 1). Increase in peak intensity could be due to the mass diffusion across the grain boundaries and crystal growth [18]. An increase in grains into larger ones (grain size incraese) after irradiation can also cause increase in peak intensity (Fig. 1) [23]. Since interstitial diffusion of oxygen atoms/ions induces micro-strain defects, these induced defects cause reduction in the crystallite size [23, 24]. However, in our case, a reduction in strain is seen after irradiation. This can be due to the annealing effect after irradiations (since irradiation can generate tremendous heat and pressure within the track or zone of ion as is discussed in the below paragraph). In present films, the defects and stresses are produced due to present growth conditions and are subsequently annealed and relaxed after ion beam irradiation. These results are well in agreement with change in the surface morphology.

As already described above, with the ion fluence, the grain size and intensity of diffraction peak increase. The SHI irradiations can drastically alter material characteristics in a narrow cylindrical region around its path. The SHI losses significant part of energy in interaction with atoms through electron–ion interaction [17]. This causes a tremendous heating in localized part of material by a phenomenon known as thermal spike, due to energy and momentum transfer from the excited electrons to the lattice in the cylindrical region [17]. Depending upon the energy and type of ion, two main processes can take place. One is sputtering of material or atoms if energy is low and another is diffusion within the system. More generally, it can be interpreted that as the fluence (number of ions/cm^2) enhances, they will be attached to the surface in the surrounding of each other. As a result, the generated melted region may approach with each other forming larger grains and hence increasing the grain size. The ion-induced grain growth is observed in various oxide-based materials [23, 24].

To quantitatively investigate the degree of preferred orientation, the texture coefficient $Tc(hkl)$ was calculated using the following Eq. [22];

$$T_{c(hkl)} = \frac{I(hlk)/I_0(hkl)}{1/N[\sum_N I(hlk)/I_0(hkl)]} \tag{6}$$

where $Tc(hkl)$ is the texture coefficient of the hkl plane, $I(hkl)$ is the measured intensity, $I_0(hkl)$ is the relative intensity of the corresponding plane given in PDF-2 data (the JCPS standard intensity) and N is the number of reflections. Sample with a randomly oriented crystallite presents $Tc(hkl) = 1$, and if $Tc(hkl) > 1$, then there is larger the abundance of crystallites orientation. The texture coefficient was calculated for the reflection plan (002). It was observed here that the orientation along (110) plane increases with radiation (see Table 2), and therefore, indicates the increase in crystallinity after irradiation.

3.2 AFM study

Surface topology of the pristine and irradiated films has been analyzed by AFM measurements. Figure 2 shows the AFM images of the studied thin films. The AFM studies reveal the surface of minimum roughness composed of triangular- or pyramidal-shaped grains. These triangular or pyramidal grains are uniformly distributed over the entire surface. The root mean square (RMS) and average roughness of the present thin films are 35 nm (for pristine), 29 nm (for Ni ion irradiated) and 25 nm (for Au ion irradiated), respectively. As the mass of irradiating ion increases, the roughness of the films decreases, in which reduction in size and number density of cracks is observed after ion irradiation [23, 24]. When the depositing energy increases, the atomic diffusion at material surfaces varies. Also the thermally induced shocks decrease the tensile stress in these films. Additionally, the enhanced thermal shock and stress cause reduced thermal stress cracking (Fig. 2) [19–21].

3.3 Micro-Raman study

As already discussed, SnO_2 has a tetragonal rutile crystalline structure with point group D_{4h}^{14} and space group $P4_2/mnm$. Therefore, the normal modes of vibrations at the Brillouin zone (BZ) of SnO_2 are represented by following irreducible representation [25, 27, 28]:

$$\Gamma_{\text{Raman}} = 1A_{1g} + 1A_{2g} + 1A_{2u} + 1B_{1g} + 1B_{2g} + 2B_{1u} + 1E_g + 3E_u$$

Of these modes, two are IR active (the single A_{2u} and the triply degenerated E_u mode), four modes are Raman active (three non-degenerate modes, A_{1g}, B_{1g}, B_{2g} and the doubly degenerate E_g) and two are silent (A_{2g} and B_{1u}). One A_{2u} and two E_u modes are acoustic and have transverse (TO) and longitudinal optical (LO) vibrations [27].

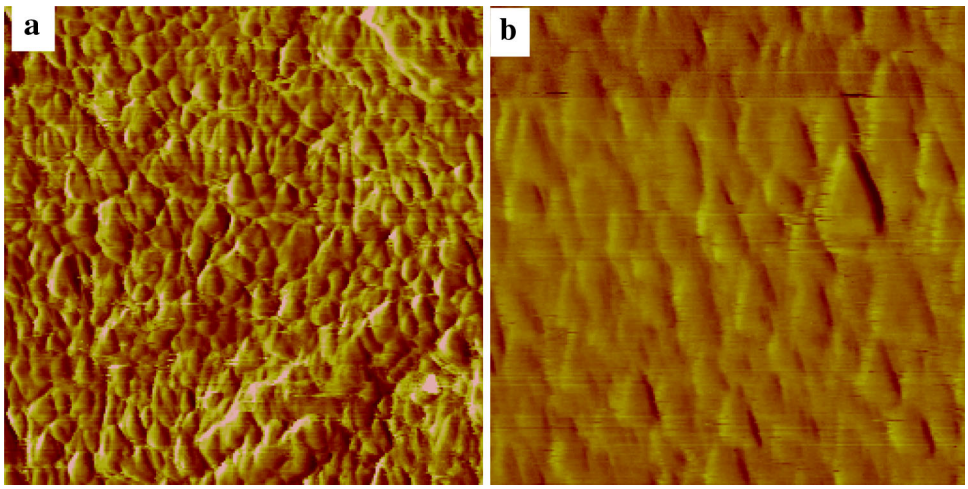

Fig. 2 AFM images of **a** Pristine and **b** Au ion irradiated films

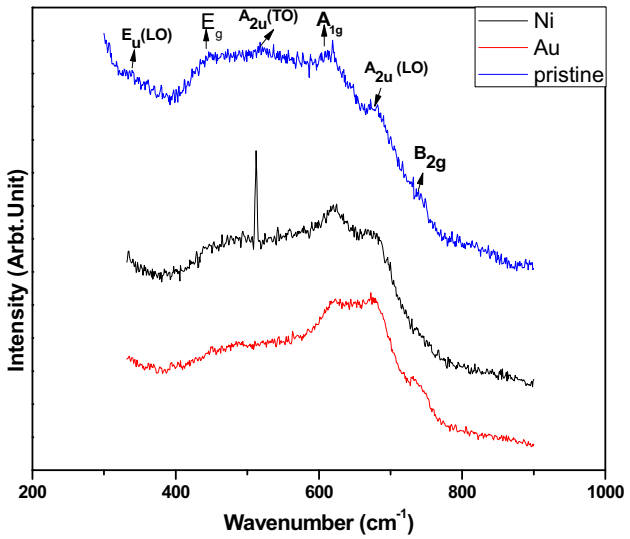

Fig. 3 Micro-Raman spectra of Pristine, Ni and Au ion irradiated films

Figure 3 shows the micro-Raman spectra of pure and irradiated Sb–SnO_2 samples. The micro-Raman spectrum of pure Sb–SnO_2 exhibits peaks and tentatively corresponding to the first group located at about 613, 450, and 749 cm^{-1}. These peaks are due to the A_{1g}, E_g and B_{2g} vibrational modes, which are in close agreement with those reported for a rutile SnO_2 single crystal [28]. We also observed other peaks located at 684, 478, 354, 242 and 292 cm^{-1}, and are tentatively related to $A_{2u}(\nu_{LO})$, $A_{2u}(\nu_{TO})$, $E_u(\nu_{2LO})$, $E_u(\nu_{TO})$ and $E_u(\nu_{LO})$ vibrational modes, respectively, corresponding to second group [26–29]. In addition, we did not observe any extra peak corresponding to any impurity or secondary phases. However, a slight variation in peak position is seen in comparison with single crystal rutile SnO_2. This observed variation is due to doping and also may be due to substrate effect (as already discussed in the XRD section of this article) [18]. Therefore, in current study, we restricted our study to higher vibrational modes only (lower part of spectrum not shown here). Therefore, more precisely, the IR bands of SnO_2 are due to (A_{2u} TO, Sn(or Sb)–O stretching), (E_u TO, Sn(or Sb)–O stretching), (A_{2u} LO, Sn–O stretching) and (E_u LO, Sn(or Sb)–O stretching) [25–30]. Also, the main characteristic Raman bands of SnO_2 are due to (B_{1g}, vibrational), (E_g, translational), (A_{1g}, symmetric Sn(or Sb)–O stretching) and (B_{2g}, asymmetric Sn(or Sb)–O stretching) [25–30]. Further, it was noted that after doping or irradiations, the peak broadening and intensity variation are observed, indicating that microstructural transformations occurred. However, as in the case of XRD measurements, no additional peaks typical of the incorporation of Sb in the SnO_2 matrix or after ion irradiations were observed. This variation in the intensity of the Raman peaks could be related to the changes in the grain size of the irradiated samples with respect to the unirradiated ones, as the lattice parameters showed only small variations with the Sb concentrations and as well as ion irradiations [23]. All these vibrational modes become quite visible in irradiated films giving us clear indication of impact of pressure generated due to the ion irradiation and its influence on Sn(or Sb)–O bond. It is well known that in an infinite perfect crystal only the phonons near the center of the *BZ* ($q_0 \approx 0$) contribute to the scattering of incident radiation due to the momentum conservation rule between phonons and incident light. Due to size effect (nano formation due to doping and irradiations), which gives rise to breakdown of the phonon momentum selection rule $q_0 \approx 0$, allowing phonons with $q \neq 0$ to contribute to the Raman spectrum [23]. This could also lead to the alterations (or shifting) of observed Raman peaks. This phonon momentum selection rule can also give rise to evolution of some silent IR modes (as 512 cm^{-1} observed in our Ni ion irradiated films).

From Raman spectra of these samples, it is observed that after irradiation few peaks become sharp. These bands correspond to Sn–O bond length and may be altered by SHI. Also, the atomic spacing distribution may be changed by ion irradiation in Sb–SnO_2 thin films. In addition, some other dominant peaks related to the given structure become visible (due to breakdown of the phonon momentum selection rule). This sharpness of peaks is an indication of increase in grain size or less disorder after irradiation. It is believed that SHI irradiations can generate or anneal out defects or disorder the system [17]. However, this modification of system mostly depends on the nature and energies of irradiating ion. In the present case, a modification in crystal structure after irradiation can be seen. Therefore, it can be concluded that present irradiating ion species can work as an effective tool to modify the given structure.

3.4 UV–Vis study

Figure 4 shows the UV–Vis spectra of pristine and irradiated Sb–SnO_2 films. The fundamental absorption, which corresponds to electron excitation from the valence band to the conduction band, can be used to determine the nature and value of the optical band gap. In the region of the fundamental absorption, the absorption coefficient (α) is given by the formula [30]:

$$(\alpha h\nu)^{\zeta} = A\left(h\nu - E_g\right) \tag{7}$$

where A is a constant, E_g is the energy gap and $\zeta = 2$ for direct allowed transitions. Inset of Fig. 4 shows $(\alpha h\nu)^2$ versus $h\nu$ (or Tauc plots) plots in the region of the fundamental absorption for all the studied samples. A linear relationship is obtained and hence predicting a direct energy band gap for the present films. The values of E_g determined from the intersection of the straight line with the $h\nu$ axis for all studied samples are listed in Table 2. They fall in the range 2.81–3.99 eV. The literature value of E_g shows wide dispersion between different investigators [31–35]. This observed dispersion can be due to two opposing factors: (a) the Moss–Burstein shift (band filling) causes a UV shift of the optical band gap and (b) the many body interaction leads to reduction in gap due to the appearance of band tails (Urbach tail). The high-energy irradiation-induced lattice damage creates defect energy states below conduction band and hence affects the band gap. The high-energy irradiation induces band-tailing effects, which seriously affect the properties of most of the semiconductor [33, 34].

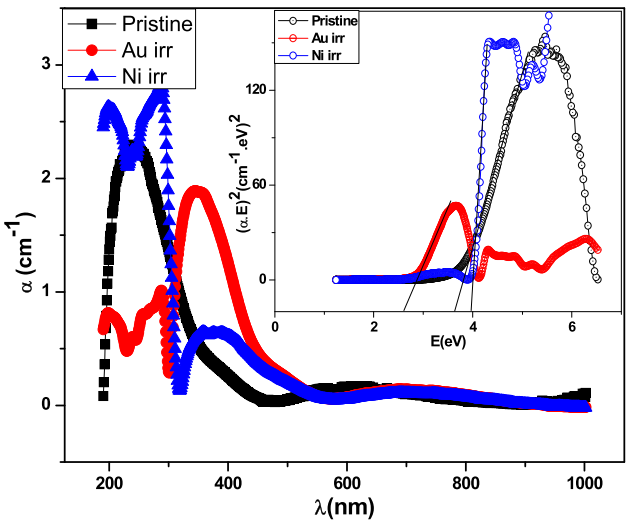

Fig. 4 UV–Visible spectra of Pristine, Ni and Au ion irradiated films. Inset shows their respective Tauc plots for optical band gap determination

The Urbach band tail (also called defect tail) was also observed in the present case. It should be noted that the various factors such as the carrier phonon interaction, carrier–impurity interaction and structure disorder are chief contributors for the Urbach band tail in semiconductors [30]. The Urbach energy (E_u) (the energy associated with this defect tail is called as Urbach energy) for the present films was determined using Urbach rule [30]:

$$\alpha = \alpha_0 \exp(h\upsilon)/E_u \tag{8}$$

where α_0 is the pre-exponential absorption coefficient factor. The values of the E_u give the more details about the optical behavior of the system. Here, we have evaluated the Urbach band tails by fitting the absorption coefficient (α) as a function of photon energy ($h\upsilon$) in the near of the fundamental absorption edge (plot not shown here). The values of E_u were determined from the inverse slope of the straight line, representing $ln(\alpha)$ versus photon energy ($h\upsilon$). The values of this activation energy are given in Table 3. A variation in E_u is seen with ion species (see Table 3). With irradiation, a decrease in E_u is seen (see Table 3). Therefore, as the E_g changes, so the magnitude of defect energy (E_u) also changes. This supports our argument that sub-band states formed in between the valence and conduction bands leading in the alteration of the E_g. In the present system, the number of defect levels below the conduction band increases (due to the mass and hence momentum or energy of ion) to such an extent that the band edge is shifted deep into the forbidden gap, thereby leading to variation in E_g. Hence, it clearly demonstrated that the enhancement or reduction in existing defects or disorder after irradiation may be the prime reason for the current observed phenomenon.

The width of the edge E_u can also be related to another parameter called steeper constant at RT by following equation [36]:

Table 3 Various optical parameters of the Pristine, Ni and Au ion irradiated films

Sample	Optical band gap E_g (eV)	Urbac energy E_u (eV)	Steeper constant (β)
Virgin	3.67	0.221	0.1176
Au ion irradiated	2.81	0.057	0.4561
Ni ion irradiated	3.99	0.044	0.5811

$$\beta = k_B T / E_u \quad (9)$$

An increase in β is seen with irradiation (see Table 3). Here, we should mention that the characterizing broadening of the optical absorption edge (Urbach edge) is due to electron phonon or exciton–phonon interactions existing in the material. Therefore, we can conclude that the SHI irradiation can be used to tune the optical band gap of the oxide materials.

3.5 Conclusion

Sb-doped SnO_2 thin films on quartz substrate were prepared by electron beam evaporation technique. These thin films were irradiated with 120 MeV Ni and Au ions at 1×10^{13} ions/cm^2. Oxide phase formation was confirmed by XRD and Raman studies. The XRD pattern reveals that pristine and irradiated films belong to tetragonal structure. This crystal structure is retained even after irradiations. The Raman data also support the projected symmetry. The particle size and stress increase with irradiation. The improvement in structure is also supported by both above-mentioned techniques. From optical data, these films shows indirect allowed transitions and a significant variation in optical band gap is observed after irradiations. From the present observations, it is concluded that a particular ion can be used as an effective tool to tune the various physical properties of some specific materials.

Acknowledgments Author K. M. Batoo is thankful to the King Abdul Aziz City of Science and Technology for providing the financial support under the project Code: MP-32-35. Author F. A. Mir would also like to thank University Grants Commission (UGC) for awarding the UGC-Dr. D. S. Kothari Postdoctoral Fellowship. Authors are thankful to the director and scientific staff of IUAC New Delhi for providing beam time facility.

References

1. D.L. Hall, A.A. Wang, K.T. Joy, T.A. Miller, M.S. Wooldridge, J. Am. Ceram. Soc. **87**, 2033 (2004)
2. B. Grzeta, E. Tkalcec, C. Goebbert, M. Takeda, M. Takahashi, K. Nomura, M. Jaksic, J. Phys. Chem. Solids **63**, 765 (2002)
3. B. Yoo, K. Kim, S.H. Lee, W.M. Kim, N.G. Park, Sol. Energy Mater. Sol. Cells **92**, 873 (2008)
4. T. Krishnakumar, R. Jayaprakash, N. Pinna, A.R. Phani, M. Passacantando, S.J. Santucci, Phys. Chem. Solids **70**, 993 (2009)
5. X.D. Xiao, G.P. Dong, J.D. Shao, H.B. He, Z.X. Fan, Appl. Surf. Sci. **256**, 1636 (2010)
6. X.J. Feng, J. Ma, F. Yang, F. Ji, F.J. Zong, C. Luan, H.L. Ma, Appl. Surf. Sci. **254**, 6601 (2008)
7. S.Y. Lee, B.O. Park, Thin Solid Films **510**, 154 (2006)
8. J.H. Lee, Thin Solid Films **516**, 1386 (2008)
9. J.K. Suna, B.V. Velamakannib, W.W. Gerbericha, L.F.J. Francis, J. Colloid Interface Sci. **280**, 387 (2004)
10. D.K. Avasthi, G.K. Mehta, *Swift heavy ions for materials engineering and nanostructuring* (Springer, Dordrecht, 2011)
11. D. Kanjilal, Curr. Sci. **80**, 1560 (2001)
12. T. Mohanty, P.V. Satyam, D. Kanjilal, J. Nanosci. Nanotechnol. **6**, 2554 (2006)
13. S. Rani, Somnath, C. Roy, N.K. Puri, M.C. Bhatnagar, D. Kanjilal, J. Nanomater. Article ID 395490 (2008)
14. N.G. Deshpande, R. Sharma, Curr. Appl. Phys. **8**, 181 (2008)
15. K.M. Abhirami, P. Matheswaran, B. Gokul, R. Sathyamoorthy, D. Kanjilal, K. Asokan, Vacuum **90**, 39 (2013)
16. A. Sharma, K.D. Verma, M. Varshney, D. Singh, M. Singh, K. Asokan, R. Kumar, Radiat. Eff. Defects Solids **165**(12), 930 (2010)
17. Ziegler JF, Biersack JP, Littmark U. The stopping range of ions in solids (Tarrytown: Pergamon) (1985); Ziegler JF (2006) http://www.srim.org
18. H. Kim, A. Pique, Appl. Phys. Lett. **84**, 218 (2004)
19. C. Terrier, J.P. Chatelon, J.A. Roger, R. Berjoan, C.J. Dubois, Sol-Gel Sci. Technol. **10**, 75–81 (1997)
20. C. Terrier, J.P. Chatelon, R. Berjoan, J.A. Roger, Thin Solid Films **263**, 37–41 (1995)
21. Feroz A. Mir, Khalid M. Batoo, Indrajeet Chatterjee, G. M. Bhat, J. Mater Sci. Mater Electron. 25:1564–1570 (2014)
22. B.D. Cullity, *Elements of X-ray diffraction*, 2nd edn. (Addison-Wesley, Massachusetts, 1978)
23. F.A. Mir, M. Ikram, R. Kumar, Appl. Radiat. Isot. **70**, 2409–2415 (2012)
24. F.A. Mir, Phil. Mag. **94**(3), 331–344 (2014)
25. A.C. Fischer-Cripps, *Nanoindentation* (Springer, New York, 2002)
26. J. Zuo, C. Xu, X. Liu, C. Wanga, C. Wang, Y. Hu, Y. Qian, J. Appl. Phys. **75**(3), 1835 (1994)
27. Diéguez A, Romano-Rodriguez A, Morante J, Weimar U, Schweizer-Berberich M, Göpel W (1996) Sens Actuators B 31:1
28. M. Batzill, U. Diebold, Progr Surf Sci **79**, 47 (2005)
29. O. Lupan, L. Chow, G. Chaic, A. Schulte, S. Park, H. Heinrich, Mater. Sci. Eng., B **157**, 101 (2009)
30. N.F. Mott, E.A. Davis, *Electronic processes in non-crystalline materials*, 2nd edn. (Clarendon Press, Oxford, 1979)
31. J.L. Jacquemin, G. Brodure, J. Phys. Chem. Solids **12**, 4767 (1979)
32. C. Kilic, A. Zunger, Origin of coexistence of conductivity and transperancy in SnO_2. Phys. Rev. Lett. **88**, 095501 (2002)
33. K.L. Narayanan, K.P. Vijayakumar, K.G.M. Nair, N.S. Thampi, Phys. B **240**, 8 (1997)
34. B. Alterkop, N. Parkansky, S. Goldsmith, R.L. Boxman, Appl. Phys. A **36**, 552 (2003)
35. K.P. Misra, R.K. Shukla, A. Srivastava, A. Srivastava, Appl. Phys. Lett. **95**, 031901 (2009)
36. H. Mahr, Phys. Rev. **125**, 1510 (1962)